Environmental Science & Technology

pubs.acs.org/est

Article

# New Insights into Calcite Dissolution Mechanisms under Water, Proton, or Carbonic Acid-Dominated Conditions

Kyung Tae Kim, Graeme Henkelman, Lynn E. Katz, and Charles J. Werth*

Cite This: *Environ. Sci. Technol.* 2024, 58, 11331−11341

Read Online

ACCESS | Metrics & More | Article Recommendations | Supporting Information

**ABSTRACT:** Carbonate minerals are ubiquitous in nature, and their dissolution impacts many environmentally relevant processes including preferential flow during geological carbon sequestration, pH buffering with climate-change induced ocean acidification, and organic carbon bioavailability in melting permafrost. In this study, we advance the atomic level understanding of calcite dissolution mechanisms to improve our ability to predict this complex process. We performed high pressure and temperature (1300 psi and 50 °C) batch experiments to measure transient dissolution of freshly cleaved calcite under $H_2O$, $H^+$, and $H_2CO_3$-dominated conditions, without and with an inhibitory anionic surfactant present. Before and after dissolution experiments, we measured dissolution etch-pit geometries using laser profilometry, and we used density functional theory to investigate relative adsorption energies of competing species that affect dissolution. Our results support the hypothesis that calcite dissolution is controlled by the ability of $H_2O$ to preferentially adsorb to surface Ca atoms over competing species, even when dissolution is dominated by $H^+$ or $H_2CO_3$. More importantly, we identify for the first time that adsorbed $H^+$ enhances the role of water by weakening surface Ca−O bonds. We also identify that $H_2CO_3$ undergoes dissociative adsorption resulting in adsorbed $HCO_3^-$ and $H^+$. Adsorbed $HCO_3^-$ that competes with $H_2O$ for Ca acute edge sites inhibits dissolution, while adsorbed $H^+$ at the neighboring surface of $CO_3$ enhances dissolution. The net effect of the dissociative adsorption of $H_2CO_3$ is enhanced dissolution. These results will impact future efforts to more accurately model the impact of solutes in complex water matrices on carbonate mineral dissolution.

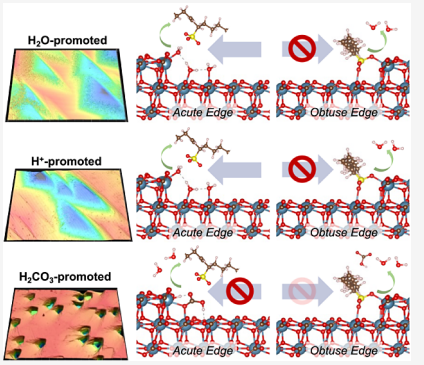


**KEYWORDS:** *calcite dissolution, dissolution inhibition, HPHT, laser profilometry, density functional theory, anionic surfactant*



## 1. INTRODUCTION

Carbonate minerals (hereafter carbonates) are ubiquitous in nature and are often subject to undersaturated waters that promote their dissolution. The most common carbonates are calcite, aragonite, and dolomite, which represent nearly 20% by volume of Phanerozoic sedimentary rock. Calcite and aragonite are comprised of only $CaCO_3$, while dolomite is a calcium and magnesium carbonate ($CaMg(CO_3)_2$). Carbonates occur mainly in sedimentary rock and aquatic environments, often comprising large fractions of these systems.[1] Important examples include carbonate-rich lake and ocean sediments, soils, fresh groundwater aquifers, shale formations, and deep saline aquifers. Both natural and anthropogenic perturbations can introduce undersaturated waters into these systems and promote carbonate mineral dissolution, where dissolution rates are impacted by water quality including specific solutes that can promote or inhibit dissolution.[2] Carbonate mineral dissolution affects a myriad of processes in natural and engineered systems including $CO_2$ flux to the atmosphere from thawing permafrost,[3] pH buffering and carbonate calcification by marine animals (e.g., corals) with climate-change induced ocean acidification,[4] sinkhole formation in limestone formations,[5] and formation or caprock permeability during geological carbon sequestration.[6] A variety of models have been proposed to describe carbonate mineral dissolution, but an atomic level understanding of how promoters and inhibitors affect carbonate mineral dissolution is lacking. This makes it challenging to predict how variations in water chemistry affect dissolution in natural systems.

In this work, we focus on advancing a mechanistic understanding of calcite dissolution. While other carbonate minerals are important, calcite is the most well studied, and this allows us to build on prior efforts. Calcite dissolution has been described by three parallel reactions, which involves the proton ($H^+$), carbonic acid ($H_2CO_3$*), and water ($H_2O$),[7,8] where $H_2CO_3$* represents the sum of both aqueous $CO_2$ and $H_2CO_3$ ($[H_2CO_3^*] = ([CO_2(aq)] + [H_2CO_3])$. These reactions are

Received: January 5, 2024
Revised: May 28, 2024
Accepted: May 29, 2024
Published: June 22, 2024

$$CaCO_3 + H^+ \underset{k_{-1}}{\overset{k_1}{\rightleftharpoons}} Ca^{2+} + HCO_3^- \quad (1)$$

$$CaCO_3 + H_2CO_3^* \underset{k_{-2}}{\overset{k_2}{\rightleftharpoons}} Ca^{2+} + 2HCO_3^- \quad (2)$$

$$CaCO_3 + H_2O \underset{k_{-3}}{\overset{k_3}{\rightleftharpoons}} Ca^{2+} + HCO_3^- + OH^- \quad (3)$$

The overall reaction in the system $H_2O-CO_2-CaCO_3$ can be written as

$$CaCO_3 + CO_2 + H_2O \leftrightharpoons Ca^{2+} + 2HCO_3^- \quad (4)$$

The net rate of dissolution for reactions 1−3 has been expressed as

$$R = k_1 a_{H^+} + k_2 a_{H_2CO_3^*} + k_3 a_{H_2O} - k_4 a_{Ca^{2+}} a_{HCO_3^-} \quad (5)$$

where $k_1$, $k_2$, and $k_3$ are temperature-dependent first-order rate constants and $k_4$ is a temperature-dependent second-order rate constant.[8] The relative contribution of each reactant is dependent on the chemical environment, specifically, on pH and $pCO_2$. Far from equilibrium and at sufficiently low pH (<5) and low $pCO_2$, the activity of $H^+$ is relatively high and the first term on the right-hand side (RHS) of eq 5 controls the overall reaction rate. At circumneutral pH and low $pCO_2$, the $H^+$ activity is negligible, and the third term on the RHS of eq 5 controls the overall reaction rate. At sufficiently low pH and high $pCO_2$, the concentration of $H_2CO_3$* is high relative to the concentration of $H^+$, and the second term of the RHS of eq 5 controls the overall reaction rate. Close to equilibrium, the fourth term on the RHS of eq 5 can be important and promotes precipitation, but this condition is not considered in this work. For all three dissolution scenarios, rhombohedral etch pits are thought to form during dissolution, each with two acute and two obtuse edges and three types of kink sites where edges meet. The overall rate of etch pit growth is a function of individual rate constants and solution activities of $H^+$, $H_2O$, and $H_2CO_3$*, and relevant environmental conditions exist where any one of these solution activities can dominate net dissolution rates. When the volume of solution to surface area of mineral (V/A) is small, such that consumption of $CO_2$ during dissolution is significant enough to lower the concentration of $CO_2$ in the solution, hydration of $CO_2$ to form $H_2CO_3$ can also be a rate limiting step.[9,10]

Prior studies have evaluated the effects of inorganic divalent metal ions (e.g., $Mg^{2+}$, $Sr^{2+}$, $Mn^{2+}$) and organic ions (e.g., amino acids, carboxylic acids, surfactants) on etch pit formation in calcite, in some cases using vertical scanning interferometry (VSI) or atomic force microscopy (AFM) to probe propagation rates of etch pits at acute and obtuse leading edges.[11−15] Both inorganic and organic ions can preferentially bind at one or more edge or kink sites during dissolution, and as a result inhibit rhombohedral etch pit growth.[13,15] When growth is inhibited more at one edge or kink site than at another, a distorted rhombohedral etch pit occurs. For example, 1 mM of $Mg^{2+}$ inhibited etch pit growth along the obtuse edge, which was attributed to preferential adsorption of $Mg^{2+}$ at this site.[13,15] The presence of organic molecules can also result in varied etch pit morphology depending on their functional groups. For example, 100 mM aspartic acid inhibited etch pit growth along acute edges, which was attributed to stronger interaction of aspartic acid at acute−acute kink compared to acute-obtuse and obtuse−obtuse kink sites.[16] Also, the presence of the anionic surfactant internal olefin sulfonate (IOS) C15−18 resulted in smaller but more dense etch pit formation in calcite at ambient pressure and temperature with $H_2O$-dominated dissolution kinetics.[17]

A number of atomic level simulations including molecular dynamics (MD) and density functional theory (DFT) calculations have been performed to unravel the mechanisms of calcite dissolution and precipitation, along with their corresponding kinetics.[18−22] These efforts include investigation of the structure of water molecules on the calcite surface, in conjunction with X-ray reflectivity (XR) and surface X-ray diffraction (SXRD).[21,23−26] Building on this foundational work, several $H_2O$-promoted dissolution models have been proposed based on experimental evidence and MD or DFT calculations, as well as surface complexation models (SCM). Shiraki et al. proposed, based on AFM results, that dissociative adsorption of water followed by nucleophilic attack by water breaks the bond between Ca and O of carbonate, which leads to a detachment of a hydrated $[HCO_3{\cdot}Ca]^+$ ion pair.[27] Ion pairs are crucial not only in dissolution but also in precipitation processes. For instance, MD simulation results by De La Pierre et al. suggested that the adsorption of ion pair $[Ca^{2+}{\cdot}CO_3^{2-}]$ to calcite edges are more favorable compared to that of the individual ions (i.e., $Ca^{2+}$, $CO_3^{2-}$).[22] Miyata et al. proposed two dissolution models that predict the formation of intermediate species during dissolution. In the first model, dissociative adsorption of water forms surface Ca associated with $OH^-$ and surface $HCO_3^-$. $HCO_3^-$ desorbs from the surface and dissociates to $CO_2$ and $OH^-$ immediately. $OH^-$ adsorbs to the surface Ca again and forms $Ca(OH)_2$, which then desorbs from the surface. The second model is similar to the first, but neglects the dissociation of $HCO_3^-$ to $CO_2$ and $OH^-$. Instead, $Ca(OH)^+$ and $HCO_3^-$ both desorb from the surface.[19,20] Models consistent with water adsorption and dissociation have also been proposed using surface complexation theory (e.g., ref 28) and the presence of surface > CaOH and > $CO_3H$ sites was experimentally identified using infrared (IR) spectroscopy[29,30] and X-ray photoelectron spectroscopy (XPS).[31] To date, however, a number of atomic simulations[26,32] revealed conflicting results that dissociative adsorption is not favored on calcite surfaces. An exception was found when water adsorbed to surface carbonate vacancy sites on the calcite (104) surface.[32] While some controversy remains, these models all assume that the availability of water at active dissolution sites is essential, and adsorption of water occurs before dissociation and dissolution.

There has been limited work to extend atomic level dissolution models to consider the effects of inhibitory molecules. However, in a related effort, De Leeuw and Cooper investigated the inhibitory effects of organic molecules with carboxylic groups on calcite precipitation by comparing the adsorption energies of the organic molecules and water. They asserted that in order for the organic molecules to be effective inhibitors, their adsorption energy must be greater than water, thereby forming more thermodynamically stable surfaces that inhibit water access to Ca and $CO_3$ at the calcite surface.[33] From these results, we infer that competitive adsorption of


https://doi.org/10.1021/acs.est.4c00162
Environ. Sci. Technol. 2024, 58, 11331−11341

additives and dissolution promotors (i.e., $H^+$, $H_2CO_3$*, $H_2O$) is a key to understanding dissolution mechanisms and the effects of additives on calcite dissolution. To the best of our knowledge, only adsorption of water to defect sites (i.e., edge and kink sites) has been studied, while adsorption of carbonic acid and protons has not. This represents an important knowledge gap given the large number of systems where carbonic acid and proton-promoted dissolution are likely to dominate (e.g., acid mine drainage, $CO_2$-enhanced oil recovery, geological $CO_2$ storage, etc.) and the potential for gleaning new mechanistic insights from these dissolution promoters.

The objectives of this study are to elucidate the mechanisms of calcite dissolution and the inhibitory effects of IOS under $H_2O$, $H^+$, and $H_2CO_3$*-dominated dissolution conditions. IOS was chosen because we used it previously to probe $H_2O$-promoted calcite dissolution under ambient temperature and pressure; it remains an ion (i.e., unprotonated) over the pH range considered in this work, and both natural and synthetic surfactants are ubiquitous in the environment.[17] To address the objectives, conditions that promote $H_2O$, $H^+$, or $H_2CO_3$*-dominated dissolution with or without IOS were created by using a high pressure and high temperature (HPHT) reaction cell containing freshly cleaved calcite, and solution phase $Ca^{2+}$ was monitored to quantify the extents of dissolution. Resulting etch pit morphologies were imaged using laser profilometry. Site-specific adsorption energies of IOS and the three dissolution promoters (i.e., $H_2O$, $H^+$, and $H_2CO_3$*) were calculated and compared at each etch pit site using DFT calculations. Overall, our results indicate that calcite dissolution requires preferential adsorption of water to proceed under all conditions, including proton and carbonic acid dominated dissolution.

## 2. MATERIALS AND METHODS

**2.1. Materials.** KCl (99%, Aldrich) was used to prepare a brine. HCl (1M, 99.99%, Aldrich) was used to adjust the pH of the brine. $HNO_3$ (70%, TraceMetal grade, Fisher Scientific) was used to prepare the samples for elemental analysis. Ultrapure water with a resistivity of 18.2 MΩ·cm produced by Barnstead Nanopure (Model 7143, Thermo Scientific) was used to prepare all solutions. Optical quality calcite was purchased from Ward's Science. Internal olefin sulfonate C15−18 (30.1%, Shell Oil Company), hereafter referred to as IOS, was used as the dissolution inhibitor. The structure of IOS C15 is shown in Figure 1.

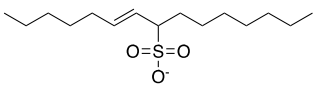


**Figure 1.** Representative structure of IOS (C15).

**2.2. High-Pressure High-Temperature Reactor Setup.** High-pressure and high-temperature experiments were carried out using a custom-built 20 mL cylindrical-shaped stainless steel reactor wrapped in heating tape. The pressure and temperature were controlled using a TELEDYNE ISCO D Series controller and the software package LabVIEW, respectively. The reactor is shown in Figure 2; it has two sapphire glass windows and four ports for (i) brine transfer, (ii) effluent sampling, (iii) gas transfer to maintain pressure, and (iv) a thermocouple. To avoid reactor corrosion and Fe leaching induced by acidic brine with a high $Cl^-$ concentration, a functionalized silica-like coating (Dursan) was applied to all reactor parts made from stainless steel (i.e., reactor, connections, and tubing) via chemical vapor deposition, and this was done by SilcoTek.

**2.3. Experimental Conditions and Dissolution Experiments.** Experimental conditions for dissolution are presented in Table 1, and either $H_2CO_3$*, $H^+$, or $H_2O$ controlled dissolution, each without or with IOS. The forward dissolution rate (e.g., $k_1a_{H^+}$) of each dissolution promotor was calculated from the activity of each promotor using the geochemical modeling program PHREEQC version 3,[34] and from the reported kinetic rate constant for each promotor.[8] Detailed PHREEQC calculations are provided in a later section. When carbonic acid controlled dissolution, brine was saturated with $CO_2$. When $H^+$ controlled dissolution, the brine pH was adjusted using HCl and pressurized with ultrahigh purity $N_2$ gas without $CO_2$. When $H_2O$ controlled dissolution, the brine was pressurized with $N_2$ without $CO_2$ at circumneutral pH. Pressure and temperature were set to 1300 psi and 50 °C for all cases, respectively. The KCl concentration was 0.401 M in all cases. The IOS concentration was always 100 mg/L when present, which is the critical micelle concentration (CMC).[17,35] The CMC was chosen because surfactants form micelles in solution and monolayers or bilayers on calcite, thereby more effectively blocking other solutes from accessing calcite and inhibiting dissolution.

Note that brines with IOS were prepared from high alkalinity IOS stock solutions stored at pH ∼ 14 for IOS stability, and special attention was required to ensure alkalinity control. Briefly, an aliquot of stock solution was diluted to 15,000 mg/L IOS, amended with HCl to reduce the pH to 4.3, and sonicated under vacuum to degas dissolved $CO_2$. The pH of the diluted solution was next adjusted to 7 by adding 0.1 M KOH. Subsequently, the diluted IOS solution was added to brine to reach 100 mg/L IOS (CMC).

For each experiment, a freshly cleaved calcite slab sample was placed in the reactor without brine. The reactor was then pressurized with $CO_2$ or $N_2$ at 1300 psi and heated to 50 °C. Brine with or without IOS was preheated and presaturated with either $CO_2$ or $N_2$ for 3 days in a presaturation vessel at the experimental pressure and temperature. The pressure of the presaturation vessel was next slightly increased to 1325 psi to induce a pressure difference between the presaturation vessel and the custom reactor. The saturated brine was then transferred to the custom reactor by opening a valve, and this initiated the experiments. $CO_2$ hydration can take tens of hours to reach equilibrium,[9] so the presaturation vessel ensures the brine is at 50 °C, saturated with $CO_2$, and in equilibrium with $H_2CO_3$, all before exposure to calcite. All experiments were duplicated for the assessment of uncertainties.

Approximately 200 μL brine samples were collected through a backpressure regulator during dissolution at 0.5, 1, 3, 6, 12, 24, and 48 h. Approximately 100 μL of each 200 μL sample were diluted into 9.9 mL of ultrapure water, mixed with 200 μL of concentrated nitric acid, and analyzed for Ca to monitor calcite dissolution. Elemental analysis was performed using a Varian 710-ES inductively coupled plasma optical emission spectroscopy (ICP-OES) instrument. The corresponding saturation state of each sample was calculated using PHREEQC. When the reaction was terminated, cleaved calcite samples were collected and dried by blowing ultrapure $N_2$ gas, and surface etch pits were evaluated using a laser profilometer.


https://doi.org/10.1021/acs.est.4c00162
Environ. Sci. Technol. 2024, 58, 11331−11341

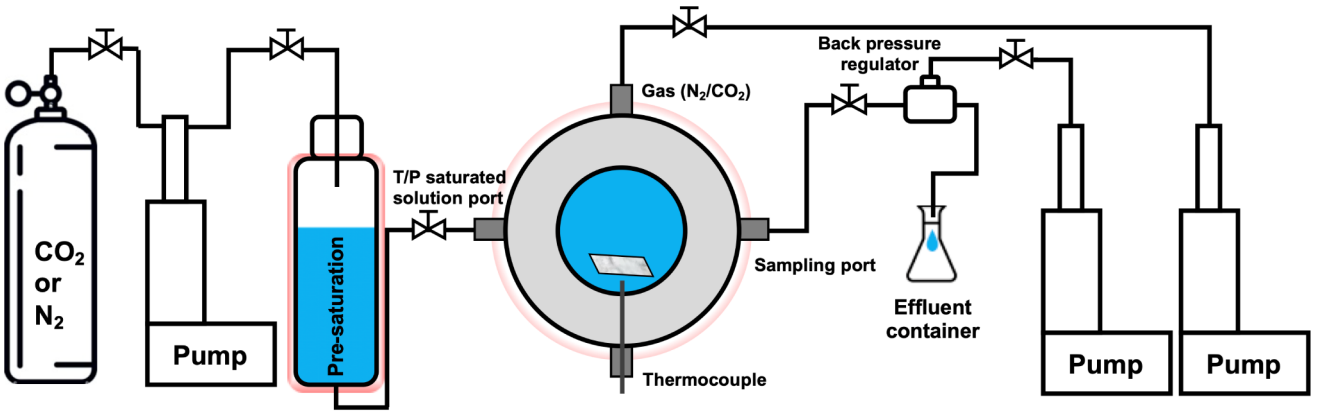


**Figure 2.** High-pressure and high-temperature experimental setup.

**Table 1. Calculated Values of Each Term in eq 5 Were Obtained Using PHREEQC Software**

| | pH | gas (P/T) | $a_{H^+}$ | $a_{H_2CO_3^*}$ | $a_{H_2O}$ | $k_1a_{H^+}$ | $k_2a_{H_2CO_3^*}$ | $k_3a_{H_2O}$ |
|---|---|---|---|---|---|---|---|---|
| $H_2CO_3$* | 3.11 | $CO_2$ (1300 psi/50 °C) | $7.82 \times 10^{-04}$ | 1.13 | $9.66 \times 10^{-01}$ | $5.20 \times 10^{-05}$ | $1.42 \times 10^{-04}$ | $3.22 \times 10^{-07}$ |
| $H^+$ | 3.12 | $N_2$ (1300 psi/50 °C) | $7.55 \times 10^{-04}$ | 0 | $9.86 \times 10^{-01}$ | $5.03 \times 10^{-05}$ | 0 | $3.28 \times 10^{-07}$ |
| $H_2O$ | 7 | $N_2$ (1300 psi/50 °C) | $9.99 \times 10^{-08}$ | 0 | $9.86 \times 10^{-01}$ | $6.65 \times 10^{-09}$ | 0 | $3.28 \times 10^{-07}$ |

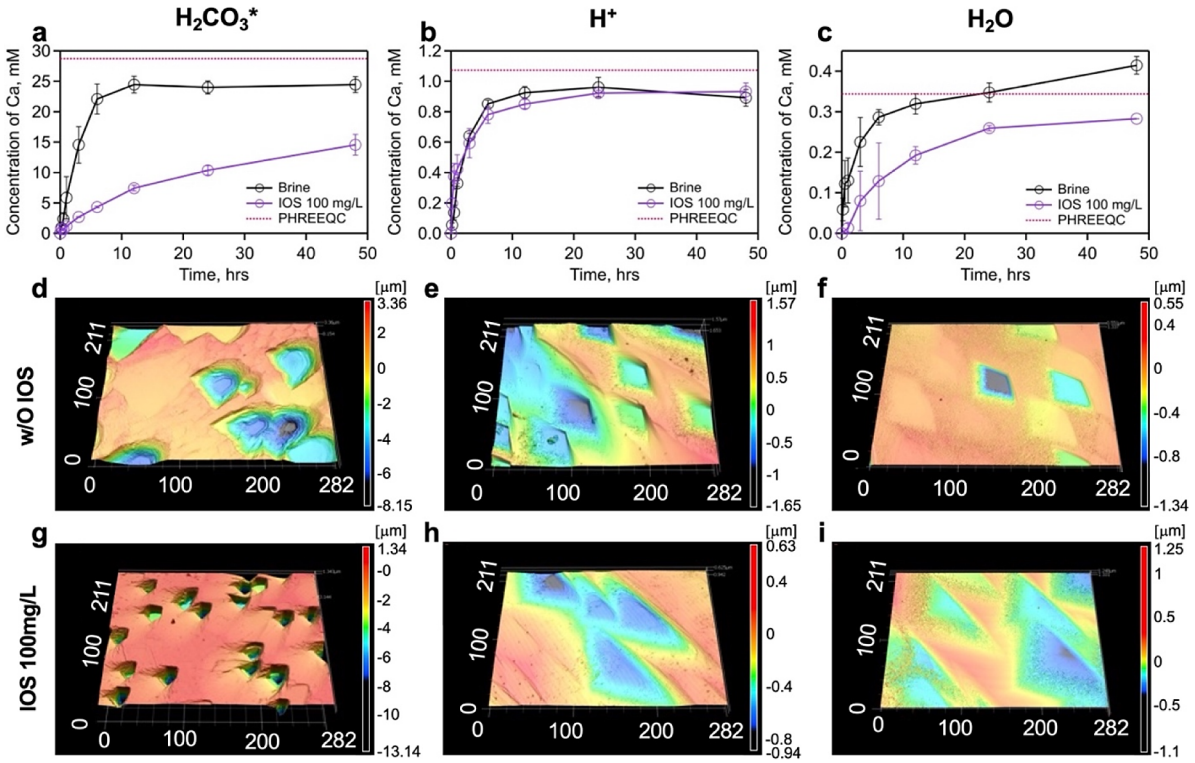


**Figure 3.** Dissolved Ca concentrations and etch pit morphologies under different chemical environments. (a−c) Dissolved Ca concentrations with and without IOS as a function of reaction time when dissolution is promoted by $H_2CO_3$* (a), $H^+$ (b), or $H_2O$ (c), respectively. (d−i) Etch pit morphology measured with a laser profilometer after reaction in brine without IOS (d−f), and with 100 mg/L of IOS (g−i). Note that only the surface profile of (d) was taken after 10 min of reaction, while those of (e−i) were taken after 48 h of reaction time. All the numbers shown in (d−i) are in μm. Corresponding experimental conditions are summarized in Table 1. All experiments were run in duplicate; error bars represent the standard deviation and the dotted line represents the theoretical equilibrium concentration of $Ca^{2+}$.

*2.3.1. Laser Profilometer.* A laser scanning confocal microscope, a Keyence VK-1100 laser profilometer, was used to obtain surface profiles of samples after dissolution experiments. All samples were rinsed with isopropyl alcohol immediately after separating from the reactor and dried using $N_2$ gas. The entire process of reactor disassembly and rinsing took less than 1 min. A 50× lens with a 0.5 nm resolution was used to scan a 211 × 281 $\mu m^2$ area. The depth and area of each pit were measured by referencing the nearby flat surface (or terrace). All surface profiles were obtained after 48 h of dissolution (Figure 3e−i), except for the $H_2CO3$*-dominated scenario without IOS. This surface profile was taken after 10


https://doi.org/10.1021/acs.est.4c00162
Environ. Sci. Technol. 2024, 58, 11331−11341

min of dissolution (Figure 3d) because high Ca concentrations at later time caused excess precipitation to occur and interfere with surface profiling when samples in the reactor were depressurized.

*2.3.2. Density Functional Theory Calculations.* Density functional theory (DFT) calculations based on the generalized gradient approximation were performed using the Vienna Ab initio Simulation Package (VASP). A plane wave basis set was used with an energy cutoff of 300 eV and a Gaussian smearing at the Fermi level with a width of 0.05 eV to improve convergence. The Perdew−Burke−Ernzerhof (PBE) functional was used to describe electron exchange and correlation.[36] The Brillouin zone was sampled at the Γ-point. The convergence criteria for electronic and geometric optimization were $10^{-6}$ eV and 0.01 eV/Å, respectively. To consider (implicit) solvent interactions, the VASPsol was used with a relative permittivity of 78.4 to mimic water.

A calcite (104) slab model of three molecular layers with a 10 Å thick vacuum layer was prepared by using a reference unit cell; the slab and specific binding sites are presented in Figure S1. An appropriate portion of Ca and $CO_3$ was removed from the top surface to build surfaces with defects including acute and obtuse edges while maintaining the entire charge at zero. For example, the acute edge model was prepared by removing half of Ca and $CO_3$ on the obtuse side of the top layer (Figure S1b). All atoms in the bottom molecular calcite layer were fixed, and the top two molecular layers were allowed to relax. A model IOS molecule was used; it has a total of 10 carbon atoms in the hydrocarbon chains, and a deprotonated form of the sulfonic acid headgroup was used because the p$K_a$ is −0.6 (methanesulfonic acid).[37] IOS and dissolution promotors (i.e., $H^+$, $H_2O$, and $H_2CO_3$) are the adsorbates; they were placed approximately 2−3 Å away from each defect site. Subsequently, all atoms except for those in the bottom layer of the calcite model were relaxed. The adsorption energies ($E_{ad}$) of each molecule were calculated based on the optimized structures using

$$E_{ad} = E_{molecule-calcite} - E_{calcite} - nE_{molecule} \quad (6)$$

where, $E_{ad}$ is the adsorption energy of an adsorbate on the calcite surface, $E_{molecule\text{-}calcite}$ is the total energy of the calcite model with adsorbate, and $E_{calcite}$ and $E_{molecule}$ are the energy of the calcite model and adsorbate, respectively; $n$ is the number of adsorbate molecules.

*2.3.3. Geochemical Modeling.* Geochemical modeling was performed using PHREEQC[34] with the *pitzer.dat* database. Major reactions considered are listed in Table S1. Fugacity coefficients were calculated with the Peng−Robinson equation of state using the critical pressure and temperature, and this provides reliable values under the studied conditions.[38] Activities of the three dissolution promotors (i.e., $H^+$, $H_2O$, and $H_2CO_3$*) corresponding to each experimental condition were calculated based on the initial solution conditions and are listed in Table 1. Whole speciation results of the initial solution conditions are summarized in Table S2. The products of activity and rate constant of the three dissolution promoters were calculated to determine the dominant promoters in solution. Based on the experimentally measured concentration of Ca, the amount of calcite to be dissolved was determined, and from this, estimated pH values at each data point were calculated.

## 3. RESULTS

**3.1. IOS Inhibits Ca Release During Calcite Dissolution Under $H_2CO_3$* and $H_2O$-dominated Conditions.** The effects of 100 mg/L (CMC) IOS on calcite dissolution were evaluated under the three rate-controlling scenarios listed in Table 1 using a custom high pressure high temperature reactor (see Methods); the Ca concentration and pH evolution over time are shown in Figures 3a-c and S2, respectively. The brine solutions for each case are initially far from equilibrium as there is no dissolved Ca. As a result, the cleaved calcite starts to dissolve and release Ca, and this release causes the rate of Ca increase in solution to slow after several hours. We note that cleaving calcite creates high energy surface sites,[39] and these sites might also dominate faster initial dissolution rates. The equilibrium concentration of Ca was estimated for each scenario using PHREEQC; this is shown in Figure 3a−c with dotted lines, and the whole speciation results are summarized in Table S3. The concentration changes of IOS were not measured; however, a decrease in IOS concentration is anticipated to be minimal since we used cleaved calcite samples rather than powered samples. To be more specific, in our prior work, we determined that each IOS molecule covers a surface area of 20.7 Å$^2$.[17] Consequently, the corresponding change in the IOS aqueous concentration when the surface is fully covered by IOS is estimated to be 0.026%, which is negligible.

Kinetic rate constants of dissolution were determined using eq 5 and the first three concentration values of Ca for each experimental data set, and the values are presented in Table 2

**Table 2. Kinetic Rate Constants Determined Using eq 5 (cm/sec)**

| | $k_1$ | $k_2$ | $k_3$ |
|---|---|---|---|
| Plummer et al.[8] | $6.66 \times 10^{-02}$ | $1.26 \times 10^{-04}$ | $3.33 \times 10^{-07}$ |
| w/o IOS (this work) | $9.99 \times 10^{-04}$ | $1.03 \times 10^{-05}$ | $6.69 \times 10^{-07}$ |
| w/IOS (this work) | $2.64 \times 10^{-03}$ | $7.88 \times 10^{-06}$ | $7.77 \times 10^{-08}$ |

along with literature values. The kinetic rate constants were calculated in the sequences of $k_3$, $k_1$, and $k_2$. The calculation began with $k_3$ using $H_2O$-dominating condition results, disregarding the minimal effects of $H_2CO_3$* and $H^+$. This initial calculation of $k_3$ informed the subsequent determination of $k_1$ and $k_2$. Specifically, $k_1$ was calculated from results under $H^+$-dominant conditions, excluding the $k_2 a_{H_2CO_3^*}$ term due to the experiments being performed under $CO_2$ free conditions. Lastly, with the obtained $k_1$ and $k_3$, $k_2$ was calculated using data from conditions dominated by $H_2CO_3$*. The relative order of rate constant values matches those in the literature, but the rate constant values from this work are less than published values, except for the $k_3$ with IOS case. One plausible reason is that the value of $k_1$ (greatest rate constant value) is affected by mass transfer limitations due to our HPHT reactor setup, and this in turn affected the value of $k_2$. Due to possible early time mass transfer limitations and possible effects of freshly cleaved calcite, we therefore focus herein on comparing the extent of dissolution at later times (e.g., 3−12 h), and not on dissolution kinetics at early time.

For $H_2CO_3$*-dominated dissolution with no IOS, the dissolved Ca concentration reaches approximately 25 mM, whereas for $H^+$ and $H_2O$-dominated dissolution, the dissolved Ca reaches 1 and 0.5 mM, respectively. The calculated


https://doi.org/10.1021/acs.est.4c00162
Environ. Sci. Technol. 2024, 58, 11331−11341

equilibrium concentrations of Ca and the corresponding equilibrium pH values for the $H_2CO_3$*, $H^+$, and $H_2O$-dominated systems are 28.74 mM at pH 4.84, 1.07 mM at pH 8.23, and 0.34 mM at pH 9.42, respectively. The greater equilibrium concentration of Ca for the $H_2CO_3$* dominated system compared to the $H^+$ dominated system at the same pH is due to the buffering capacity of the former.

When IOS was added to brine at the CMC, Ca release to solution was measurably inhibited for $H_2CO_3$* and $H_2O$-dominated dissolution, but not for $H^+$-dominated dissolution, and the extent of inhibition was greater with $H_2CO_3$*. After 48 h, the amounts of Ca release in the $H_2CO_3$* and $H_2O$-dominated scenarios with IOS still do not reach those without IOS. This selective inhibitory effect suggests that IOS adsorption to calcite hinders adsorption of $H_2CO_3$* and $H_2O$ to calcite surfaces.

**3.2. $H_2CO_3$* and IOS Alter Etch Pit Morphology.** Etch pits created during calcite dissolution experiments were probed using laser profilometry, and the results are presented in Figure 3d–i. All images in Figure 3 are oriented so that the two acute edges are always at the bottom left for ease of comparison. Since the mass of calcite dissolved from cleaved sample varies between samples, we focused on comparing etch pit shape and not size, except when comparing relative etch pit size for $H_2CO_3$*-promoted dissolution with and without IOS present.

After $H_2O$ and $H^+$-dominated dissolution of calcite without IOS, classical rhombohedral etch pits formed (Figure 3e,f), but not after $H_2CO_3$*-dominated dissolution without IOS (Figure 3d). For the latter scenario, etch pits grew toward the obtuse edge sites, resulting in an arrowhead-like or pentagon-shaped etch pit after 10 min of dissolution (Figure 3d). This anisotropic dissolution under high $pCO_2$ conditions was not previously been reported. After $H_2O$ and $H^+$-dominated dissolution of calcite with IOS, etch pits grew toward the acute edge and acute–acute kink sites but were inhibited at the obtuse edge and obtuse–obtuse kink sites, resulting in triangular etch pits. In contrast, after $H_2CO_3$*-dominated dissolution with IOS, the etch pit shapes are similar to those without IOS, but much smaller even after 48 h. The difference in etch pit shape after $H^+$-dominated dissolution without and with IOS was unexpected, because Ca release into solution did not measurably change for these two cases (Figure 3b). Hence, at the macroscopic scale, the inhibition of etch pit growth by IOS for $H^+$-dominated dissolution appears to be negligible. For $H_2O$-dominated dissolution, however, this inhibition appears to have a large effect at the macroscopic scale.

**3.3. DFT Calculations Show Dissolution Occurs When Water Preferentially Binds to Ca Surface Sites.** To augment our interpretation of the experimental results, DFT calculations were performed to probe dissolution mechanisms and site-specific inhibitory effects of IOS when dissolution is dominated by each driving species (i.e., $H^+$, $H_2CO_3$*, and $H_2O$). Note that $H_2CO_3$* activity is used in the kinetic model (eq 5) to represent the driving force for dissolution. However, the actual species that adsorbs to calcite and promotes dissolution is thought to be $H_2CO_3$,[40] so hereafter $H_2CO_3$ is used when referring to DFT calculations and results.

**3.4. Adsorption of IOS.** The binding configurations of IOS to the calcite (104) surface (terrace) and edge sites were obtained and are presented in Figures 4 and S3, and corresponding binding energies are shown in Figure 5 (purple bars). The three oxygen atoms in the sulfonate headgroup of IOS interact with surface Ca atoms and form three or fewer

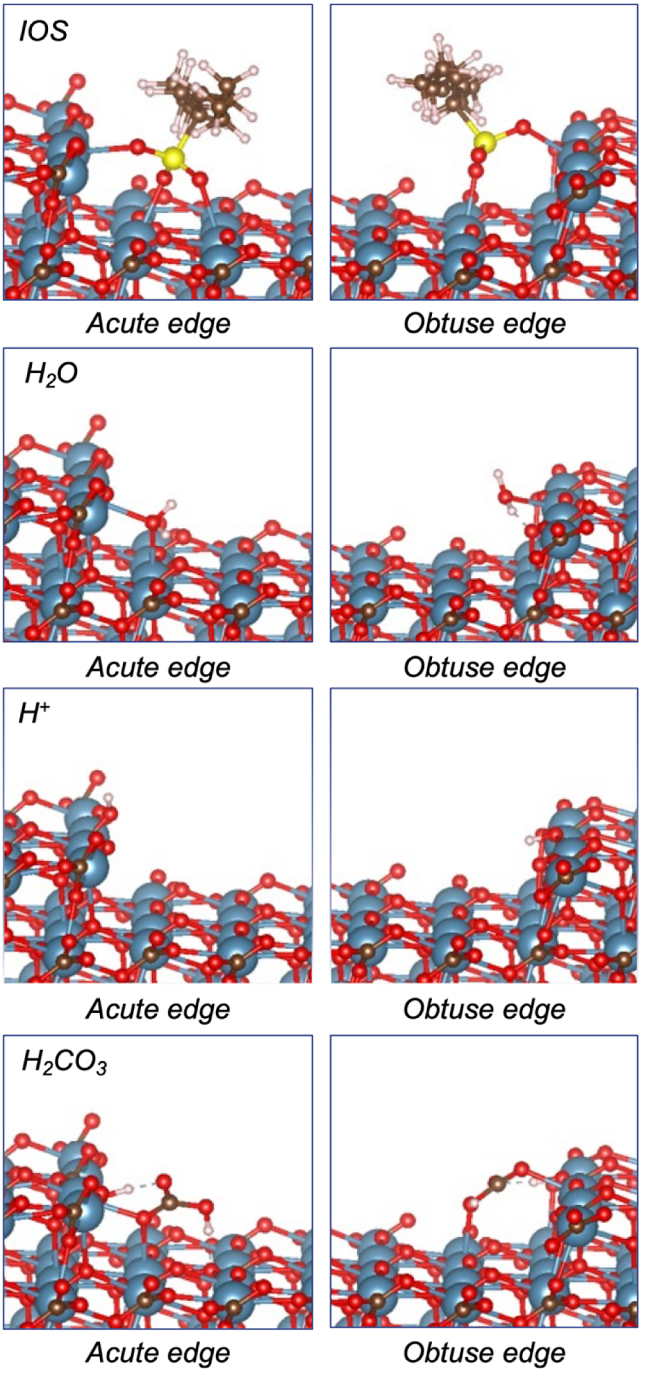


**Figure 4.** Optimized adsorption conformations of IOS, $H_2O$, $H^+$, and $H_2CO_3$ at acute and obtuse edges.

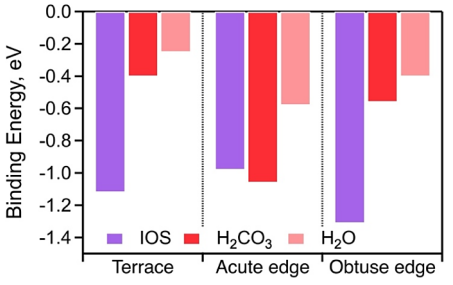


**Figure 5.** Adsorption energy IOS and dissolution promoters to calcite terrace and defect models.



https://doi.org/10.1021/acs.est.4c00162
Environ. Sci. Technol. 2024, 58, 11331–11341

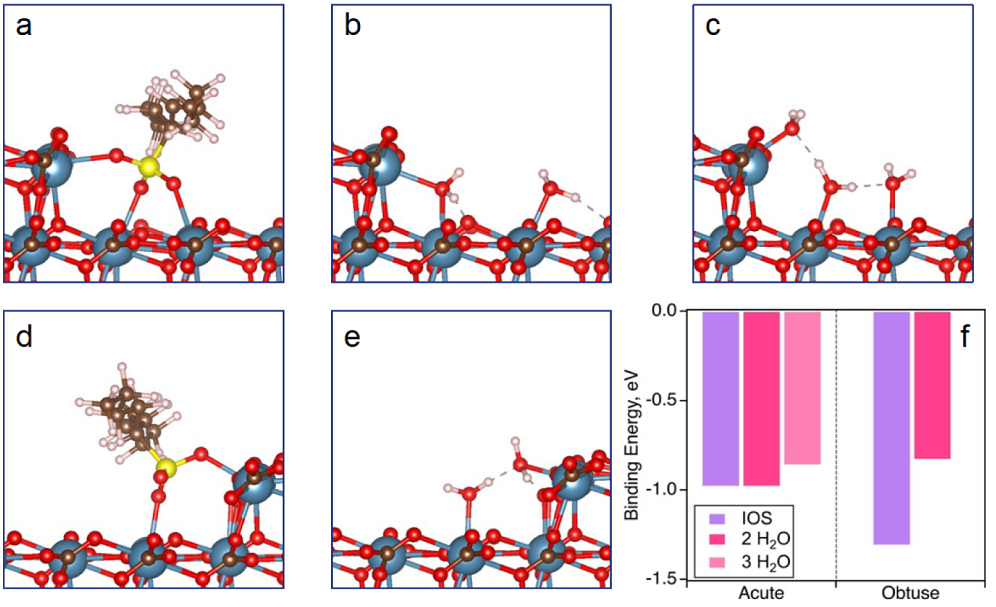


**Figure 6.** Comparison of binding energy and conformation between IOS and multiple water molecules on the acute and obtuse edges. a−c) Adsorption conformations of IOS, and $H_2O$ molecules on an acute edge, d,e) adsorption conformations of IOS, and $H_2O$ molecules on an obtuse edge, and f) comparison of adsorption energy of IOS and $H_2O$ molecule(s) on acute and obtuse edges.

bonds. At the acute edge, IOS has the least favorable bond energy (−0.98 eV), and this energy becomes more favorable with bonding to a terrace (−1.12 eV), and then the obtuse edge (−1.31 eV). The binding energy is related to both the number of atoms participating in binding and their distances to the surface. At the acute edge, each O atom in IOS interacts with one Ca atom on the slab, i.e., one O atom in the sulfonate headgroup interacts with one Ca atom on the upper slab and two O atoms each interact with one Ca atom on the lower slab; the bond distances are 2.51, 2.57, and 2.48 Å, respectively. At the obtuse edge, only two O atoms of IOS interact with Ca atoms, i.e., one O atom in the sulfonate headgroup interacts with one Ca atom on the upper slab and one O atom interacts with one Ca on the lower slab; the bond distances are shorter, at 2.38 and 2.40 Å, respectively. This indicates that for these edge sites, the distance between O atoms of the sulfonate headgroup to surface Ca atoms, and not number of Ca atoms, determines the overall binding energy. At the terrace, only one O atom of IOS participates in bonding, and the distance from that O atom to surface Ca atom is 2.39 Å (see Table S4 and Figure S3).

**3.5. Adsorption of $H_2O$ Alone and Compared to IOS.** The binding configurations of $H_2O$ to calcite terrace and defect sites were obtained and are presented in Figures 4 and S4, and corresponding binding energies are shown in Figure 5 (pink bars). For all 3 cases, the O atom of $H_2O$ primarily interacts with one or two surface Ca atoms, and the H atom weakly interacts with a neighboring O atom of surface $CO_3$. At the terrace, $H_2O$ has the least favorable bond energy (−0.25 eV), and this energy becomes more favorable with bonding to the obtuse edge and then the acute edge. As with IOS, the binding energy is related to both the number of bonding atoms and their corresponding distances. At the terrace, the O atom of $H_2O$ interacts with only one surface Ca atom on the slab, and one of the H atoms of $H_2O$ is oriented toward the protruding O atom of the surface $CO_3$ on the c-gliding plane (Figure S4); the calculated bond distances are 2.52, and 1.81 Å, respectively. Similarly, at the obtuse edge, the O atom of $H_2O$ interacts with one Ca atom on the upper slab; the bond distance is 2.43 Å. At the acute edge, the O atom of $H_2O$ interacts with one surface Ca atom on the upper slab and one on the lower slab; the average bond distance is 2.51 Å. The formation of this multiple interaction between the O atom of $H_2O$ and surface Ca atoms might be due to a steric effect. The Ca atom on the upper slab and that on the lower slab are much closer at the acute edge compared to the obtuse edge. We note that the binding conformation and trends in adsorption energy of $H_2O$ to the terrace, acute edge, and obtuse edge are consistent with results from by Lardge et al.[32] With respect to binding conformation, we highlight that $H_2O$ remains intact during binding and dissociative adsorption of $H_2O$ was not observed here as proposed elsewhere.[19,20,27] Our observations are supported by results from Andersson and Stipp,[41] who combined DFT calculations with an implicit solvent model to determine that $pK_a$'s of adsorbed $H_2O$ molecules on terrace, acute edge and obtuse edge sites are 12.7, 10.0, and 13.2, respectively, indicating that dissociative adsorption of $H_2O$ is thermodynamically unfavored under our experimental condition (Table 1). However, it is still possible that water dissociation occurs in a subsequent dissolution step when Ca−O bonds are broken.

The adsorption energies of a single IOS molecule are greater than those of a single $H_2O$ molecule for all 3 cases (Figure 5). Thus, the adsorption of IOS at first appears more thermodynamically favorable than the adsorption of $H_2O$. However, IOS and $H_2O$ interact with a different number of Ca atoms at the acute and obtuse edges, and the adsorption energies for bonding to the same number of Ca atoms at each site must be considered to determine thermodynamic favorability. At the acute edge, IOS forms three bonds with Ca atoms, whereas $H_2O$ forms two bonds with Ca atoms. At the obtuse edge, IOS forms two bonds with Ca atoms, whereas $H_2O$ forms one bond with Ca atoms. Therefore, new calculations were performed to determine the bonding energies of 2 or 3 $H_2O$ molecules together at acute and obtuse edges.


https://doi.org/10.1021/acs.est.4c00162
Environ. Sci. Technol. 2024, 58, 11331−11341

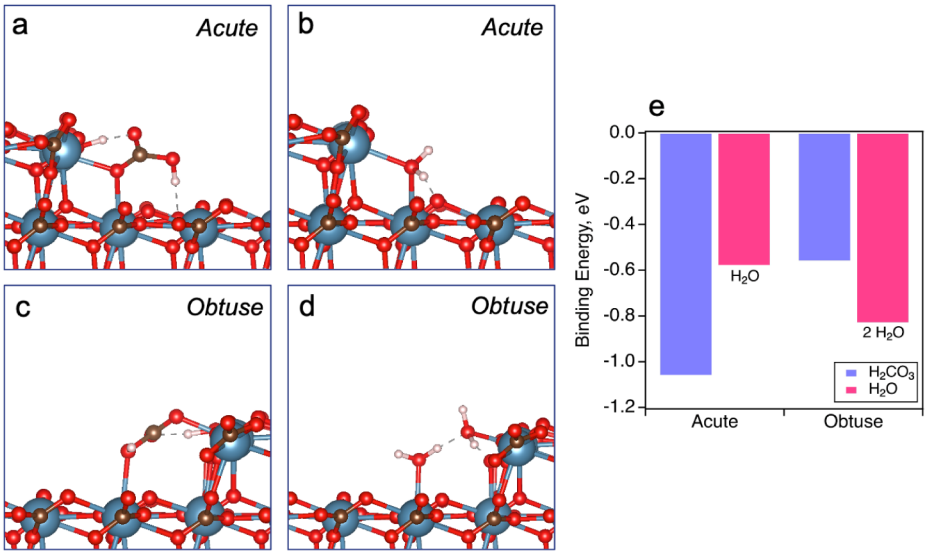


**Figure 7.** Comparison of binding energy and conformation between $H_2CO_3$ and multiple water molecules on acute and obtuse edges. Adsorption conformations of $H_2CO_3$, and $H_2O$ molecule(s) on a,b) an acute edge, c,d) an obtuse edge, and e) comparison of corresponding binding energies shown in a−d.

Each $H_2O$ molecule was initially placed on the Ca atoms that were found to interact with IOS, and subsequently relaxed. The most favorable binding configurations are presented in Figure 6b,c,e, with corresponding adsorption energies in Figure 6f. At acute edge sites, the binding energy of two $H_2O$ molecules (−0.98 eV) is identical to that of IOS, whereas at obtuse sites, the binding energy of IOS (−1.31 eV) remains favorable as compared to two water molecules (−0.83 eV). The results indicate that displacement of $H_2O$ by IOS is not thermodynamically favorable at acute edge sites but is thermodynamically favorable at obtuse edge sites. This can explain the experimental observation of triangular etch pits by obtuse edge truncation in calcite when IOS is present (Figure 3i).

**3.6. Adsorption of $H^+$ Alone and Compared to IOS.** The binding configurations of $H^+$ to edge sites were also obtained, and the results are presented in Figure 4. $H^+$ interacts with one O atom of surface $CO_3$ at all sites, and this interaction is supported by published XPS results of protonated carbonate sites ($>CO_3H^0$).[31]

The relative binding energies of $H^+$ and IOS are not compared because $H^+$ adsorbs to the O surface sites while IOS adsorbs to the Ca surface sites, suggesting these two species do not compete for the same sites on the calcite surface. This can explain why Ca release during calcite dissolution experiments in the $H^+$-dominant scenario is not affected by the presence of IOS, but not why dissolution etch pits are truncated at the obtuse edge in the presence of IOS. A reasonable explanation is that dissolution still requires $H_2O$ under $H^+$-dominated dissolution conditions, and that $H^+$ enhances $H_2O$-promoted dissolution by weakening the bond energy between Ca and O in adjacent surface carbonate ($((Ca{-}O)_n{-}C)$). This binding energy weakening is supported by DFT calculation results presented in Figure S5, which show that protonation of surface $CO_3$ resulted in longer Ca−O bond distances at both acute and obtuse edges. The requirement of $H_2O$ to promote dissolution with $H^+$ is supported by laser profilometry results that show inhibition of dissolution at the obtuse edge with $H^+$, and by DFT results indicating that IOS binds preferentially to water at this site. Interestingly, any promotional effect of $H^+$ on dissolution by $H_2O$ appear substantially greater than any inhibitory effect of IOS, given the similarity in solubilized Ca with and without IOS present under the $H^+$-dominant scenario.

**3.7. Adsorption of $H_2CO_3$ Alone and Compared to IOS.** The binding configurations of $H_2CO_3$ to the terrace, acute edge, and obtuse edge were obtained and are presented in Figures 4 and S6, and corresponding binding energies are shown in Figure 5 (red bars). One or two oxygen atoms in the $H_2CO_3$ interact(s) with surface Ca atoms and form three or fewer bonds. Dissociation of $H_2CO_3$ to $HCO_3^-$ and $H^+$ was observed except when adsorbed to the terrace. The dissociated $H^+$ adsorbs to a neighboring O atom of surface $CO_3$, and the $HCO_3^-$ adsorbed to Ca sites. At the acute edge, one of the O atoms of the dissociated $HCO_3^-$ forms two bonds with Ca atoms on the upper and lower slab; the bond distances are 2.43, and 2.48 Å, respectively. At the obtuse edge, one O atom of the dissociated $HCO_3^-$ forms a bond with a Ca atom on the upper slab, and one O atom forms a bond with a Ca atom on the lower slab; the bond distances are 2.36 and 2.61 Å, respectively. This indicates that at these edge sites, bond distances and not the number of O atoms in the $HCO_3^-$ determine the overall bond strength. At the terrace, dissociative adsorption was not observed, and one of the O atoms of $H_2CO_3$ forms a bond to a Ca atom on the surface, and a H atom attached to O in $H_2CO_3$ interacts with a neighboring O atom of $CO_3$ on the surface.

$H^+$ that dissociates from $H_2CO_3$ and binds to a neighboring O atom of surface carbonate could similarly enhance dissolution discussed via the $H^+$-promoted mechanism discussed in Section 3.6, i.e., it weakens binding between Ca−O. $HCO_3^-$, however, may have an opposite effect at acute edge sites, where laser profilometry results indicate dissolution is inhibited with or without IOS present; this is supported by the DFT results in Figure 7, which presents binding energies of $H_2CO_3$ with either one or two water molecules such that the number of bonds to Ca for these two species is matched. As shown, $H_2CO_3$ binds more strongly than $H_2O$ at the acute


https://doi.org/10.1021/acs.est.4c00162
Environ. Sci. Technol. 2024, 58, 11331−11341

edge, while $H_2O$ binds more strongly than $H_2CO_3$ at the obtuse edge. To our knowledge, we are the first to report $H_2CO_3$ dissociation to $HCO_3^-$ and $H^+$ at acute and obtuse edge sites, with corresponding preferential adsorption of $HCO_3^-$ over $H_2O$ at acute edge Ca sites, as well as adsorption of $H^+$ at the O surface sites with corresponding weakening of Ca−O bonds. We note that our results are consistent with species in carbonate mineral SCMs which assumes two primary hydration sites (i.e., $>CaOH^0$, and $>CO_3H^0$). This approach assumes $H^+$-promoted dissolution is governed by protonated surface carbonate sites ($>CO_3H^0$) at pH < 5, and $H_2O$-promoted dissolution is controlled by fully hydrated metal centers ($>CaOH_2^+$) at pH > 6. The formation of carbonated metal centers ($>CaHCO_3^0$) sacrifices the number of the fully hydrated metal centers ($>CaOH_2^+$), thereby inhibiting $H_2O$-promoted dissolution. The results of dissociative adsorption found in this study can be correlated to the surface species $>CO_3H^0$, and $>CaHCO_3^0$, which respectively promote and inhibit calcite dissolution.[42−44]

Binding energies of IOS are compared to those of $H_2CO_3$ and $H_2O$ in Figure 5. IOS adsorbs less strongly than $H_2CO_3$ on the acute edge, and more strongly than either $H_2CO_3$ or $H_2O$ on the terrace or obtuse edge, suggesting that $HCO_3^-$ will continue to inhibit etch pit formation at acute edge sites even in the presence of IOS, as was observed experimentally. This also suggests that IOS should inhibit dissolution by water at terrace and obtuse edge sites, and we observed very small etch pits after 48 h in the presence of IOS compared to large etch pits observed in the absence of IOS after 10 min.

## 4. DISCUSSION

The series of experiments and DFT calculations provided direct and indirect insights into (i) the mechanisms of calcite dissolution under $H_2O$, $H^+$, and $H_2CO_3$-dominated scenarios and (ii) site-specific inhibition mechanisms by an amphiphilic organic molecule, i.e., an anionic surfactant with a sulfonate headgroup. Regarding dissolution mechanisms, the results from both experimental and DFT calculations are consistent with $H_2O$ being necessary to hydrate Ca atoms to promote calcite dissolution under all three dissolution scenarios, with $H^+$ enhancing the role of water by weakening surface Ca−O bonds, and with $H_2CO_3$ both enhancing the role of water at obtuse edge sites (via dissociation of a $H^+$) and inhibiting the role of water at acute edge sites (via dissociation of $HCO_3^-$). They (i.e., experimental and DFT results) are also consistent with $H_2O$ being necessary to hydrate Ca atoms prior to dissolution in the presence of IOS, with dissolution being inhibited by IOS at obtuse edge sites when IOS adsorbs more strongly than $H_2O$ at these sites under all three dissolution scenarios, and with dissolution proceeding in the presence of IOS at acute edge sites when IOS adsorbs more weakly than $H_2O$ at these sites under $H^+$ and $H_2O$-dominated scenarios. The IOS does not noticeably affect dissolution at acute edge sites under $H_2CO_3$-dominated conditions, because $H_2CO_3$ already inhibits $H_2O$ adsorption at this location.

As noted in the Introduction, a number of prior authors have indicated the key role of $H_2O$ in calcite dissolution, and proposed various models that generally assume $H_2O$ dissociation at the calcite surface to hydroxylate Ca (e.g., $Ca(OH)_2$) and protonate $CO_3$ (e.g., $HCO_3$)[19,20] when $H_2O$ adsorbs to a carbonate vacancy;[32] also, the presence of such surface functionality (i.e., $>CaOH^0$, $>CO_3H^0$) was experimentally detected using XPS.[31] A variation of this model was proposed by Van Cappellen et al., who proposed that the $H^+$ enhances dissolution rates when two neighboring $CO_3$ surface groups are protonated adjacent to a hydrated surface Ca ($>CaOH_2^+$).[28] Interestingly, our DFT results do not indicate $H_2O$ dissociation at the calcite surface, which is in agreement with Lardge et al.[32] However, the end product of dissolution is aqueous $Ca^{2+}$ coordinated to 6 or more water molecules,[45] with $H^+$ and $OH^-$ likely playing important roles along the way. Hence, there are many possible intermediate steps between the adsorption of one or a few water molecules at the calcite surface and the solubilization of Ca and $CO_3$, and these steps remain a topic of further study.

As also noted in the Introduction, only a few studies have extended atomic level dissolution models to consider the effects of inhibitory molecules. The general outcome has been that preferential adsorption of other species versus $H_2O$ at edge sites will dehydrate surface species.[33] This work extends understanding by showing that preferential adsorption of other species such as IOS and $HCO_3^-$ at surface Ca sites at either acute or obtuse edges will inhibit dissolution, but that preferential adsorption of other species at surface O sites (e.g., $H^+$) will not inhibit dissolution, but possibly enhance it. This is because water preferentially binds to Ca sites and the interaction of other molecules that interact with O sites can help weaken surface Ca−O bonds to promote calcite dissolution. This interpretation is not consistent with that from Subhas et al., who reported that increasing concentrations of carbonic anhydrase increase the concentration of $H_2CO_3$ at defect sites and decreases the energetic barrier to etch pit nucleation. However, these authors did not consider adsorption of specific molecules to calcite defect sites, nor did they consider $H_2CO_3$ dissociation to $H^+$ and $HCO_3^-$.[40]

We note that the mechanisms we propose are consistent with eq 5 and the associated rate constants, which increase as $k_{H_2O}(k_3) < k_{H_2CO_3^*}(k_2) < k_{H^+}(k_1)$. Specifically, water is required for dissolution in all dissolution scenarios. In the presence of $H_2CO_3$, which dissociates to $H^+$ and $HCO_3^-$ at calcite edges (Figure 7a,c), there is both an inhibitory effect of $HCO_3^-$ competing with $H_2O$ for Ca at acute edge sites, and a promotional effect of $H^+$ enhancing dissolution at obtuse edge sites, with the latter effect dominating the net dissolution kinetics and resulting in a greater dissolution rate constant. Lastly, in the presence of $H^+$, there is only the promotional effect enhancing dissolution, and this results in the greatest dissolution rate constant.

This study provides new insights into atomic level mechanisms of calcite dissolution driven by three dissolution promotors (i.e., $H_2O$, $H^+$, $H_2CO_3$), and into inhibition mechanisms of calcite dissolution by IOS. Specifically, results of this study indicate that (i) $H_2O$ is necessary to hydrate Ca atoms to promote calcite dissolution under all three dissolution scenarios. (ii) $H^+$ enhances the role of water by weakening surface Ca−O bonds. (iii) $H_2CO_3$ both enhances the role of water at obtuse edge sites (via dissociation of a $H^+$) and inhibits the role of water at acute edge sites (via dissolution of $HCO_3^-$). Further, preferential adsorption of three dissolution promotors and IOS alters etch pit morphology indicating that (i) IOS adsorbs more strongly than $H_2O$ at obtuse edge sites under all three dissolution scenarios and inhibits calcite dissolution. (ii) IOS adsorbs more weakly than $H_2O$ at acute edge sites under $H^+$ and $H_2O$-dominated scenarios and does not inhibit calcite dissolution at this location. (iii) IOS does


https://doi.org/10.1021/acs.est.4c00162
Environ. Sci. Technol. 2024, 58, 11331−11341

not affect dissolution at acute edge sites under $H_2CO_3$-dominated conditions, because $H_2CO_3$ already inhibits $H_2O$ adsorption at this location.

Overall, the results indicate that calcite dissolution is controlled by the ability of $H_2O$ to preferentially adsorb to surface Ca atoms over competing species, even when dissolution is dominated by $H^+$ or $H_2CO_3$, and that IOS is an effective inhibitor of dissolution, especially in subsurface environments where elevated $pCO_2$ is expected. They also highlight the beneficiary use of an HPHT experimental setup, which made probing these mechanisms possible. The findings of this study will aid in understanding a myriad of issues closely related to loss of carbonate minerals in environmental systems (e.g., in thawing permafrost,[3] acidifying oceans,[4,46] and limestone formations[5]), and support the use of surfactants as a potential option to mitigate these issues in engineered system (e.g., during geological carbon sequestration[6]). This work focuses exclusively on inhibition mechanisms attributed to the interaction of anionic surfactants with positively charged surface Ca ions on calcite. To better understand the dissolution mechanisms and inhibition effect by additives, further investigation is required by using cationic surfactants that might interact with negatively charged surface carbonates.

## ■ ASSOCIATED CONTENT

### Supporting Information

The Supporting Information is available free of charge at https://pubs.acs.org/doi/10.1021/acs.est.4c00162.

PHREEQC speciation results, bonds distances between IOS and $H_2O$ to calcite defect models, pH evolution, and binding configuration of IOS, $H_2O$, $H^+$, and $H_2CO_3$ (PDF)

## ■ AUTHOR INFORMATION


### Corresponding Author

**Charles J. Werth** − *Department of Civil, Architecture & Environmental Engineering, The University of Texas at Austin, Austin, Texas 78721, Unites States;* orcid.org/0000-0002-8492-5523; Email: werth@utexas.edu

### Authors

**Kyung Tae Kim** − *Department of Civil, Architecture & Environmental Engineering, The University of Texas at Austin, Austin, Texas 78721, Unites States*

**Graeme Henkelman** − *Department of Chemistry, The University of Texas at Austin, Austin, Texas 78721, United States;* orcid.org/0000-0002-0336-7153

**Lynn E. Katz** − *Department of Civil, Architecture & Environmental Engineering, The University of Texas at Austin, Austin, Texas 78721, Unites States*

Complete contact information is available at: https://pubs.acs.org/10.1021/acs.est.4c00162


### Author Contributions

K.T.K, L.E.K., and C.J.W. designed the study. K.T.K. performed the experiments and the modeling works. G.H. supervised density functional theory calculations. All authors contributed toward data interpretation and the writing of the manuscript.

### Notes

The authors declare no competing financial interest.

## ■ ACKNOWLEDGMENTS

This material is based upon work supported by the U.S. Department of Energy, Office of Science, Office of Basic Energy Sciences under Award #DE-SC0017328 and the Welch Foundation (F-1841). Computational resources were provided by the Texas Advanced Computing Center.

## ■ REFERENCES


(1) Folk, R. L. Spectral subdivision of limestone types, AAPG. 1962.

(2) Morse, J. W.; Arvidson, R. S.; Lüttge, A. Calcium Carbonate Formation and Dissolution. *Chem. Rev.* **2007**, *107* (2), 342−381.

(3) Schädel, C.; Bader, M. K.-F.; Schuur, E. A. G.; Biasi, C.; Bracho, R.; Čapek, P.; De Baets, S.; Diáková, K.; Ernakovich, J.; Estop-Aragones, C.; Graham, D. E. Potential carbon emissions dominated by carbon dioxide from thawed permafrost soils. *Nat. Clim. Change* **2016**, *6* (10), 950−953.

(4) Hoegh-Guldberg, O.; Mumby, P. J.; Hooten, A. J.; Steneck, R. S.; Greenfield, P.; Gomez, E.; Harvell, C. D.; Sale, P. F.; Edwards, A. J.; Caldeira, K.; Knowlton, N. Coral reefs under rapid climate change and ocean acidification. *Science* **2007**, *318* (5857), 1737−1742.

(5) Zhou, W.; Beck, B. F. Management and mitigation of sinkholes on karst lands: an overview of practical applications. *Environ. Geol.* **2008**, *55* (4), 837−851.

(6) Akono, A. T.; Druhan, J. L.; Dávila, G.; Tsotsis, T.; Jessen, K.; Fuchs, S.; Crandall, D.; Shi, Z.; Dalton, L.; Tkach, M. K.; et al. A review of geochemical−mechanical impacts in geological carbon storage reservoirs. *Greenhouse Gases: Sci. Technol.* **2019**, *9* (3), 474−504.

(7) Chou, L.; Garrels, R. M.; Wollast, R. Comparative study of the kinetics and mechanisms of dissolution of carbonate minerals. *Chem. Geol.* **1989**, *78* (3−4), 269−282.

(8) Plummer, L. N.; Wigley, T. M. L.; Parkhurst, D. L. The kinetics of calcite dissolution in CO 2 -water systems at 5 degrees to 60 degrees C and 0.0 to 1.0 atm CO 2. *Am. J. Sci.* **1978**, *278* (2), 179−216.

(9) Dreybrodt, W.; Lauckner, J.; Zaihua, L.; Svensson, U.; Buhmann, D. The kinetics of the reaction CO2+ H2O→ H++ HCO3− as one of the rate limiting steps for the dissolution of calcite in the system H2O CO2 CaCO3. *Geochim. Cosmochim. Acta* **1996**, *60* (18), 3375−3381.

(10) Kaufmann, G.; Dreybrodt, W. Calcite dissolution kinetics in the system CaCO3−H2O−CO2 at high undersaturation. *Geochim. Cosmochim. Acta* **2007**, *71* (6), 1398−1410.

(11) Morse, J. W.; Arvidson, R. S. The dissolution kinetics of major sedimentary carbonate minerals. *Earth-Sci. Rev.* **2002**, *58* (1−2), 51−84.

(12) Vinson, M. D.; Lüttge, A. Multiple length-scale kinetics: an integrated study of calcite dissolution rates and strontium inhibition. *Am. J. Sci.* **2005**, *305* (2), 119−146.

(13) Arvidson, R. S.; Collier, M.; Davis, K. J.; Vinson, M. D.; Amonette, J. E.; Luttge, A. Magnesium inhibition of calcite dissolution kinetics. *Geochim. Cosmochim. Acta* **2006**, *70* (3), 583−594.

(14) Vinson, M. D.; Arvidson, R. S.; Luttge, A. Kinetic inhibition of calcite (104) dissolution by aqueous manganese(II). *J. Cryst. Growth* **2007**, *307* (1), 116−125.

(15) Xu, M.; Higgins, S. R. Effects of magnesium ions on near-equilibrium calcite dissolution: Step kinetics and morphology. *Geochim. Cosmochim. Acta* **2011**, *75* (3), 719−733.

(16) Wu, C.; Zhao, K.; Wang, X.; Cao, M.; Xu, H.; Lu, J. R. Dissolution of the Calcite (104) Face under Specific Calcite−Aspartic Acid Interaction As Revealed by in Situ Atomic Force Microscopy. *Cryst. Growth Des.* **2012**, *12* (5), 2594−2601.

(17) Kim, K. T.; Jagannath, M. S. P.; Su, G. M.; Freychet, G.; Zeng, T.; Mohanty, K. K.; Henkelman, G.; Katz, L. E.; Werth, C. J. Surfactant inhibition mechanisms of carbonate mineral dissolution in shale. *Colloids Surf., A* **2021**, *625*, 126857.

(18) Armstrong, B. I.; Silvestri, A.; De La Pierre, M.; Raiteri, P.; Gale, J. D. Determining the Complete Stability of Calcite Kink Sites: Real vs Ideal. *J. Phys. Chem. C* **2023**, *127* (28), 13958−13968.

(19) Miyata, K.; Takeuchi, K.; Kawagoe, Y.; Spijker, P.; Tracey, J.; Foster, A. S.; Fukuma, T. High-Speed Atomic Force Microscopy of the Structure and Dynamics of Calcite Nanoscale Etch Pits. *J. Phys. Chem. Lett.* **2021**, *12* (33), 8039−8045.
(20) Miyata, K.; Tracey, J.; Miyazawa, K.; Haapasilta, V.; Spijker, P.; Kawagoe, Y.; Foster, A. S.; Tsukamoto, K.; Fukuma, T. Dissolution Processes at Step Edges of Calcite in Water Investigated by High-Speed Frequency Modulation Atomic Force Microscopy and Simulation. *Nano Lett.* **2017**, *17* (7), 4083−4089.
(21) Raiteri, P.; Gale, J. D. Structure and Dynamics of Water at Step Edges on the Calcite {10$\bar{1}$4} Surface. *Cryst. Growth Des.* **2016**, *16* (10), 5907−5914.
(22) De La Pierre, M.; Raiteri, P.; Stack, A. G.; Gale, J. D. Uncovering the atomistic mechanism for calcite step growth. *Angew. Chem., Int. Ed.* **2017**, *56* (29), 8464−8467.
(23) Brugman, S. J. T.; Raiteri, P.; Accordini, P.; Megens, F.; Gale, J. D.; Vlieg, E. Calcite (104) Surface−Electrolyte Structure: A 3D Comparison of Surface X-ray Diffraction and Simulations. *J. Phys. Chem. C* **2020**, *124* (34), 18564−18575.
(24) Reischl, B.; Raiteri, P.; Gale, J. D.; Rohl, A. L. Atomistic Simulation of Atomic Force Microscopy Imaging of Hydration Layers on Calcite, Dolomite, and Magnesite Surfaces. *J. Phys. Chem. C* **2019**, *123* (24), 14985−14992.
(25) Söngen, H.; Schlegel, S. J.; Tracey, J.; Hosseinpour, S.; Hwang, D.; Bechstein, R.; Bonn, M.; Foster, A. S.; Kühnle, A.; et al. Water Orientation at the Calcite-Water Interface. *J. Phys. Chem. Lett.* **2021**, *12* (31), 7605−7611.
(26) Fenter, P.; Kerisit, S.; Raiteri, P.; Gale, J. D. Is the calcite−water interface understood? Direct comparisons of molecular dynamics simulations with specular X-ray reflectivity data. *J. Phys. Chem. C* **2013**, *117* (10), 5028−5042.
(27) Shiraki, R.; Rock, P. A.; Casey, W. H. *Aquat. Geochem.* **2000**, *6* (1), 87−108.
(28) Van Cappellen, P.; Charlet, L.; Stumm, W.; Wersin, P. A surface complexation model of the carbonate mineral-aqueous solution interface. *Geochim. Cosmochim. Acta* **1993**, *57* (15), 3505−3518.
(29) Kuriyavar, S. I.; Vetrivel, R.; Hegde, S. G.; Ramaswamy, A. V.; Chakrabarty, D.; Mahapatra, S. Insights into the formation of hydroxyl ions in calcium carbonate: Temperature dependent FTIR and molecular modelling studies. *J. Mater. Chem.* **2000**, *10* (8), 1835−1840.
(30) Neagle, W.; Rochester, C. H. Infrared study of the adsorption of water and ammonia on calcium carbonate. *J. Chem. Soc., Faraday Trans.* **1990**, *86* (1), 181.
(31) Stipp, S. L.; Hochella, M. F. Structure and bonding environments at the calcite surface as observed with X-ray photoelectron spectroscopy (XPS) and low energy electron diffraction (LEED). *Geochim. Cosmochim. Acta* **1991**, *55* (6), 1723−1736.
(32) Lardge, J. S.; Duffy, D. M.; Gillan, M. J.; Watkins, M. Ab Initio Simulations of the Interaction between Water and Defects on the Calcite (10$\bar{1}$ 4) Surface. *J. Phys. Chem. C* **2010**, *114* (6), 2664−2668.
(33) De Leeuw, N. H.; Cooper, T. G. A Computer Modeling Study of the Inhibiting Effect of Organic Adsorbates on Calcite Crystal Growth. *Cryst. Growth Des.* **2004**, *4* (1), 123−133.
(34) Parkhurst, D. L.; Appelo, C. *Description of input and examples for PHREEQC version 3 : A computer program for speciation, batch-reaction, one-dimensional transport, and inverse geochemical calculations* US Geological Survey; 2013, 497
(35) Zeng, T.; Kim, K. T.; Werth, C. J.; Katz, L. E.; Mohanty, K. K. Surfactant Adsorption on Shale Samples: Experiments and an Additive Model. *Energy Fuels* **2020**, *34* (5), 5436−5443.
(36) Perdew, J. P.; Burke, K.; Ernzerhof, M. Generalized Gradient Approximation Made Simple. *Phys. Rev. Lett.* **1996**, *77* (18), 3865−3868.
(37) Bordwell, F. G. Equilibrium acidities in dimethyl sulfoxide solution. *Acc. Chem. Res.* **1988**, *21* (12), 456−463.
(38) Anabaraonye, B. U.; Crawshaw, J. P.; Trusler, J. P. M. Brine chemistry effects in calcite dissolution kinetics at reservoir conditions. *Chem. Geol.* **2019**, *509*, 92−102.
(39) Hakim, S. S.; Olsson, M. H. M.; Sørensen, H. O.; Bovet, N.; Bohr, J.; Feidenhans'l, R.; Stipp, S. L. S. Interactions of the calcite {10.4} surface with organic compounds: Structure and behaviour at mineral−organic interfaces. *Sci. Rep.* **2017**, *7* (1), 7592.
(40) Subhas, A. V.; Adkins, J. F.; Rollins, N. E.; Naviaux, J.; Erez, J.; Berelson, W. M. Catalysis and chemical mechanisms of calcite dissolution in seawater. *Proc. Natl. Acad. Sci. U. S. A.* **2017**, *114* (31), 8175−8180.
(41) Andersson, M. P.; Stipp, S. L. S. How acidic is water on calcite? *J. Phys. Chem. C* **2012**, *116* (35), 18779−18787.
(42) Pokrovsky, O. S.; Schott, J. Surface Chemistry and Dissolution Kinetics of Divalent Metal Carbonates. *Environ. Sci. Technol.* **2002**, *36* (3), 426−432.
(43) Pokrovsky, O. S.; Golubev, S. V.; Schott, J. Dissolution kinetics of calcite, dolomite and magnesite at 25 C and 0 to 50 atm pCO2. *Chem. Geol.* **2005**, *217* (3−4), 239−255.
(44) Pokrovsky, O. S.; Golubev, S. V.; Schott, J.; Castillo, A. Calcite, dolomite and magnesite dissolution kinetics in aqueous solutions at acid to circumneutral pH, 25 to 150 C and 1 to 55 atm pCO2: New constraints on CO2 sequestration in sedimentary basins. *Chem. Geol.* **2009**, *265* (1−2), 20−32.
(45) Katz, A. K.; Glusker, J. P.; Beebe, S. A.; Bock, C. W. Calcium Ion Coordination: A Comparison with That of Beryllium, Magnesium, and Zinc. *J. Am. Chem. Soc.* **1996**, *118* (24), 5752−5763.
(46) Sulpis, O.; Boudreau, B. P.; Mucci, A.; Jenkins, C.; Trossman, D. S.; Arbic, B. K.; Key, R. M. Current $CaCO_3$ dissolution at the seafloor caused by anthropogenic $CO_2$. *Proc. Natl. Acad. Sci. U. S. A.* **2018**, *115* (46), 11700−11705.


https://doi.org/10.1021/acs.est.4c00162
*Environ. Sci. Technol.* 2024, 58, 11331−11341